Supplementary Information (SI) for Journal of Materials Chemistry A.

A synergistic catalyst of C_{60}-confined Ag_3Fe_2 and dual-metal sites for breaking activity and stability trade-off for oxygen reduction

Rong Jin[1, 4], Chaozhong Guo*[1], Yujun Si* [2], Yao Liu[1], Liumei Teng[1], Feiling Fu[1], Yang Jian[1], Xiaoyu Dong[3], Tatyana Grigorievna Cherkasova*[4]

[1]College of Materials Science and Engineering, Chongqing University of Arts and Sciences, Chongqing 402160, China

[2]College of Chemistry and Environmental Engineering, Sichuan University of Science and Engineering, Zigong 643000, China

[3]Faculty of Chemistry and Engineering, Xinjiang Institute of Engineering, Xinjiang, 830023, China

[4]Institute of Chemical and Gas and Oil Technologies, T.F. Gorbachev Kuzbass State Technical University, Kemerovo 650000, Russia

1. Chemicals

Zinc acetate dehydrate ($(CH_3COO)_2Zn{\cdot}2H_2O$) was acquired from Chengdu Kelong Chemical Reagent Factory. Silver acetate (CH_3COOAg), 2-methylimidazole (2-MIM), hemin chloride($C_{34}H_{31}ClFeN_4O_4$), ammonia ($NH_3{\cdot}H_2O$) and hydrofluoric acid (HF) were purchased from Shanghai Aladdin Biochemical Technology Co., Ltd. Nanoclay ($H_4Al_2O_9Si_2$) is from Sigma-aldrich. Ultrapure water is self-made in the laboratory.

2. Catalysts preparation

A) Synthesis of precursor FeAg-N-C: $C_{34}H_{31}ClFeN_4O_4$ (0.06 mmol) and $H_4Al_2O_9Si_2$ (0.14 mmol) were dissolved in 30 mL $NH_3{\cdot}H_2O$ via Ultrasonic-dispersion. Then ultrapure water (50 ml) was adding the mixed solution to form homogeneous solution. Next, CH_3COOAg (0.18 mmol) was fully dissolved in the above-mentioned solution. $(CH_3COO)_2Zn\cdot 2H_2O$ (3.6 mmol) was further added to the mixed solution. The mixture was stirred at room temperature for 10min. Finally, 2-MIM (30 mmol) was joined in the mixture solution and stirred for 12h at 30 °C. The as-obtained samples were centrifuged, frozen into ice and freezing-drying for 8h. The corresponding green product was denoted as precursor AgFe-N-C.

The precursor FeAg-N-C was transferred into a corundum crucible and put into a tube furnace to be pyrolyzed from room temperature to at 350 °C for 1 h and 1000 °C for 2 h with a ramp rate of 5 $°C \cdot min^{-1}$ under N_2 gas flow, finally cooled to room temperature naturally. Next, the obtained black product was immersed and stirred in 40% HF for 6 h to clear the free metal species and nanoclay, and then repeatedly washed by deionized water and dried at 60 °C for 12 h. For the sake of repairing the carbon structure destroyed during the pickling, an additional heat treatment was carried out at 900 °C under N_2 flow for 1 h. Finally, the target catalyst FeAg-N-C was prepared.

B) Preparation of Fe-Ag-N-C catalysts: The synthesis method of Fe-Ag-N-C is consistent with that of FeAg-N-C. The difference is that Fe-Ag-N-C does not stay at a low temperature of 350 °C during pyrolysis, but directly heats up to 900 °C and holds for 2 hours. The remaining steps are the same to obtain the catalyst Fe-Ag-N-C.

C) Preparation of catalyst Ag-N-C and Fe-N-C: As controls, catalyst Ag-N-C was fabricated by the same method, except for $C_{34}H_{31}ClFeN_4O_4$. Catalyst Fe-N-C was also prepared by the similar way to not added CH_3COOAg in the solution.

3. Characterization

The morphology, elemental composition, and crystal structure of the materials were analyzed employing a scanning electron microscope (Gemini, SEM-300) and a transmission electron microscope (TEM, FEI-F30). Next, in order to observe internal structure of FeAg-N-C catalysts more clearly, which were observed by high-angle annular dark-field scanning transmission electron microscopy (HAADF/STEM) using a JEM-200F instrument. The crystalline structure evolution of the FeAg-N-C catalyst during pyrolysis was investigated using a high-temperature *in-situ* X-ray diffraction (D8 ADVANCE, Bruker, 30 kV, Cu Kα radiation) under a continuous high-purity N_2 atmosphere. The crystalline phase of catalysts was checked by X-ray diffraction (XRD) on a diffractometer (D8 ADVANCE, Bruker). The Raman spectra were recorded with 532 nm laser excitation to characterize the defect structures of the catalysts and monitor the evolution of ORR intermediates on the electrode surface. BET tests were performed using ASAP 2460 instrument to analyze the specific surface area and pore size of various materials. X-ray photoelectron spectroscopy (XPS) was performed using a Thermo 250Xi instrument to characterize the elemental composition of the materials. The X-ray absorption spectroscopy (XAS) measurements, including both X-ray absorption near-edge structure (XANES) and extended X-ray absorption fine structure (EXAFS), were conducted at the Fe K-edge and Ag K-edge using the synchrotron radiation source (SSLS). The acquired spectra were subsequently processed and analyzed following standard protocols using the ATHENA module within the IFEFFIT software package. Inductively coupled plasma-optical emission spectroscopy (ICP-OES) was performed on the FeAg-N-C material using an Agilent ICPOES 730 instrument.

4. Catalyst evaluation

All electrochemical measurements were performed on a CHI760E electrochemical workstation (Chenhua, China) with a three-electrode system, in which a glassy carbon electrode, an Hg/HgO electrode in saturated KOH solution, and a Pt foil were used as the working electrode, reference electrode, and counter electrode, respectively. O_2 saturated 0.1 M KOH electrolyte served as the electrolyte. The rotating disk electrode

(RDE) and the rotating ring disk electrode (RRDE) were polished to mirror-like surface. Catalyst inks were prepared by dispersing 1 mg materials in a solvent mixture consisting of deionized water (160 μL), ethanol (20 μL) and Nafion (20 μL), followed by sonication to form homogeneous suspension. Then the catalysts suspension was loaded on RDE by 15 μL. For comparison, commercial 20 wt.% Pt/C was also measured with the same procedure. The cyclic voltammetry (CV) measurements for ORR activity were conducted at a scan rate of 50 mV s^{-1}, and the Linear Sweep Voltammetry (LSV) curves were recorded at a rate of 5 mV s^{-1}. All the measured potentials were converted to the reversible hydrogen electrode (RHE) reference scale based on the equation:

$$E_{\mathrm{RHE}} = E_{\mathrm{Hg/HgO}} + 0.8663\ \mathrm{V}$$

Electrochemical active surface area (ECSA) was measured by CV of catalyst carried out in a potential range of 0.9163~1.0163 V (vs. RHE), at 2, 4, 6, 8, 10, 12 and14 mV s^{-1} of scan rate. The fitted slope between current densities with scan rates is the electrical double layer capacitance (C_{dl}). The higher C_{dl} represents the greater ECSA of the catalyst. The ORR stability of catalyst was recorded by chronoamperometric responses (*i-t* curves) at 0.60 V (vs. RHE). Rotating ring disk electrode measurement was performed at a rotating speed of 1,600 rpm with a scan rate of 10 mV s^{-1}. The yield of hydrogen peroxide (%H_2O_2) and the electron transfer number (n) in ORR were calculated using the equations below:

$$\%H_2O_2 = 100\frac{2j_r/N}{j_d + (j_r/N)}$$

$$n = 4\frac{j_d}{j_d + (j_r/N)}$$

Herein, j_d and j_r are the current densities on disk and ring electrodes, respectively. N is the collection efficiency of ring electrode (N = 0.37).

The Koutecky-Levich plots were collected at different rotational speed to analyze the kinetic activities and the electron transfer number (*n*). The equation is as follows:

$$\frac{1}{j}=\frac{1}{j_k}+\frac{1}{j_L}=\frac{1}{j_k}+\frac{1}{Bw^{-1/2}}$$

$$B=0.2nFC_0D_0^{2/3}U^{-1/6}$$

Here, j, j_k, and j_L are the measured, kinetic-limiting, and diffusion limiting current densities, respectively. ω is the rotating speed in rpm, F is the Faraday constant (96485 C mol^{-1}), C_0 is the oxygen concentration (1.26×10^{-6} mol cm^{-3}), D_0 is the diffusion coefficient of oxygen (1.9×10^{-5} cm^2 s^{-1}) in 0.1 M KOH, and υ is the kinetic viscosity (0.01 cm^2 s^{-1}) of 0.1 M KOH.

The homemade Zn-air battery was assembled with a polished zinc foil as anode and carbon paper coated with catalyst (1.0 mg cm^{-2}) as the air cathode. 6.0 M KOH served as electrolyte while the battery was discharged. The mixture of 6.0 M KOH and 0.2 M $Zn(Ac)_2$ served as electrolyte in charge/discharge cycles. The galvanostatic charge/discharge cycling measurements were collected on a CT-4008 testing system (Neware, China) at a current density of 10 mA cm^{-2}. Flowing O_2 was afforded at 80 mL min^{-1} during the test process.

Supplementary Figures and Tables

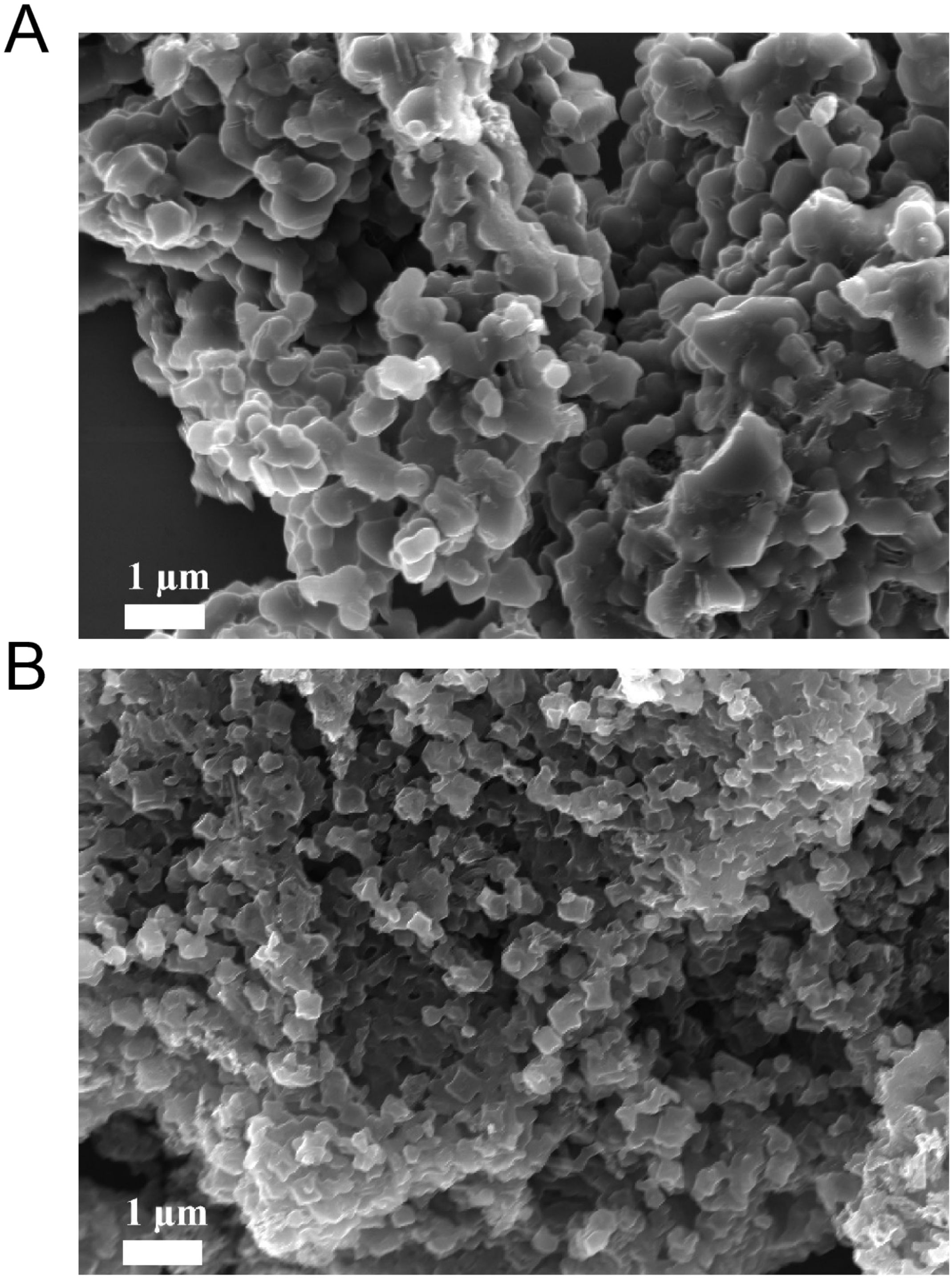

Figure S1 (A-B) SEM images of Ag-N-C and Fe-N-C

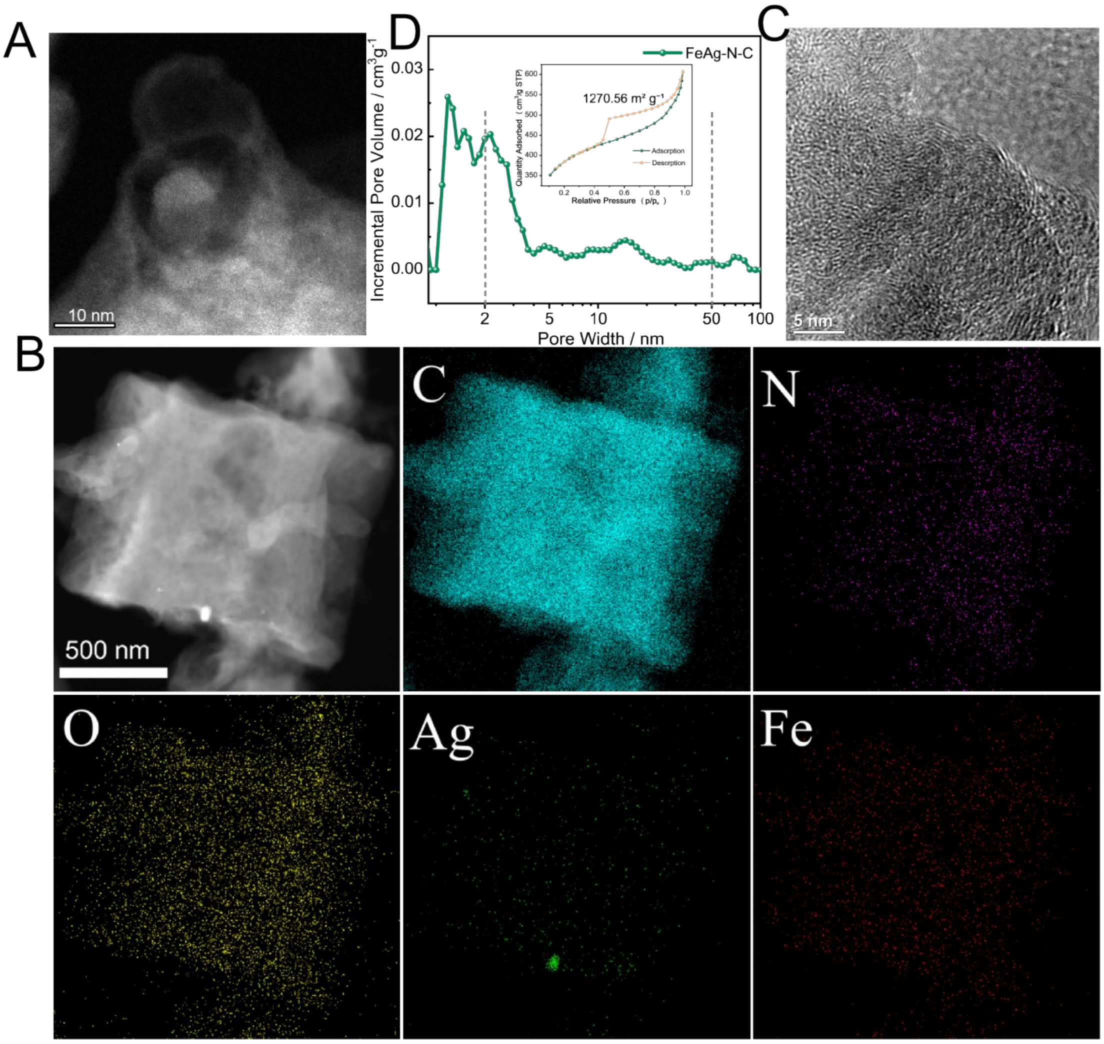

Figure S2 (A) C60-like graphitic layers surrounding the metal particle; (B) EDS images of FeAg-N-C. (C) TEM; (D) Pore distributions of FeAg-N-C.

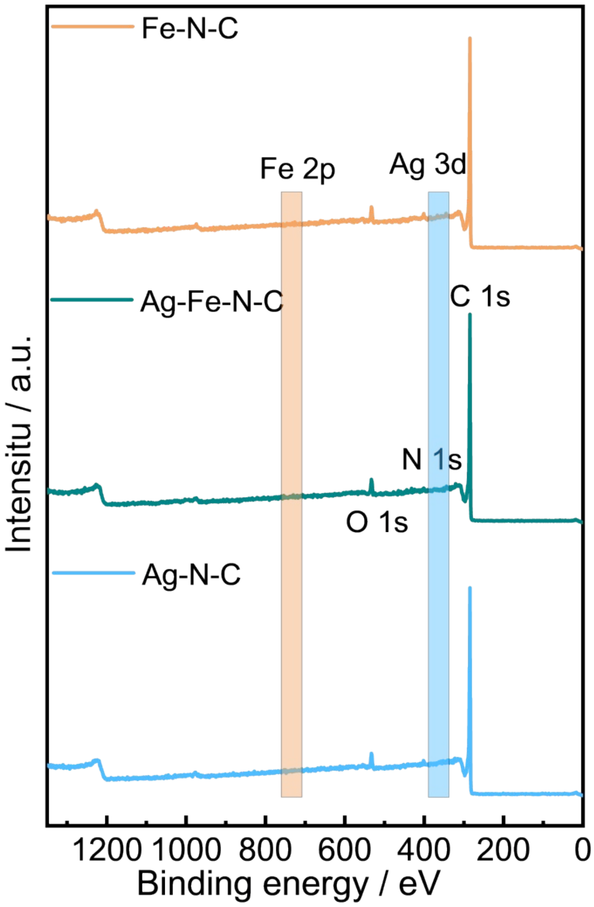

Figure S3 The XPS survey spectra of FeAg-N-C, Ag-N-C and Fe-N-C.

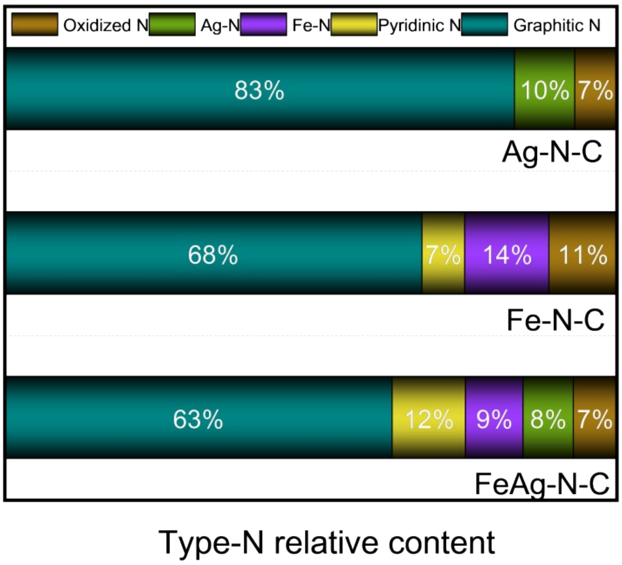

Figure S4 The content Ns of AgFe-N-C, Fe-N-C and Ag-N-C.

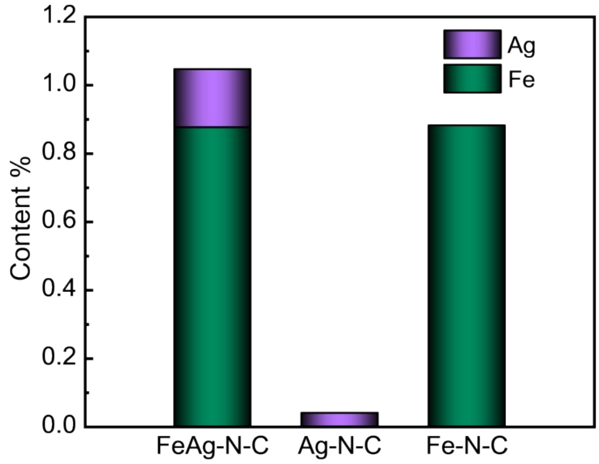

Figure S5 ICP of FeAg-N-C, Ag-N-C and Fe-N-C.

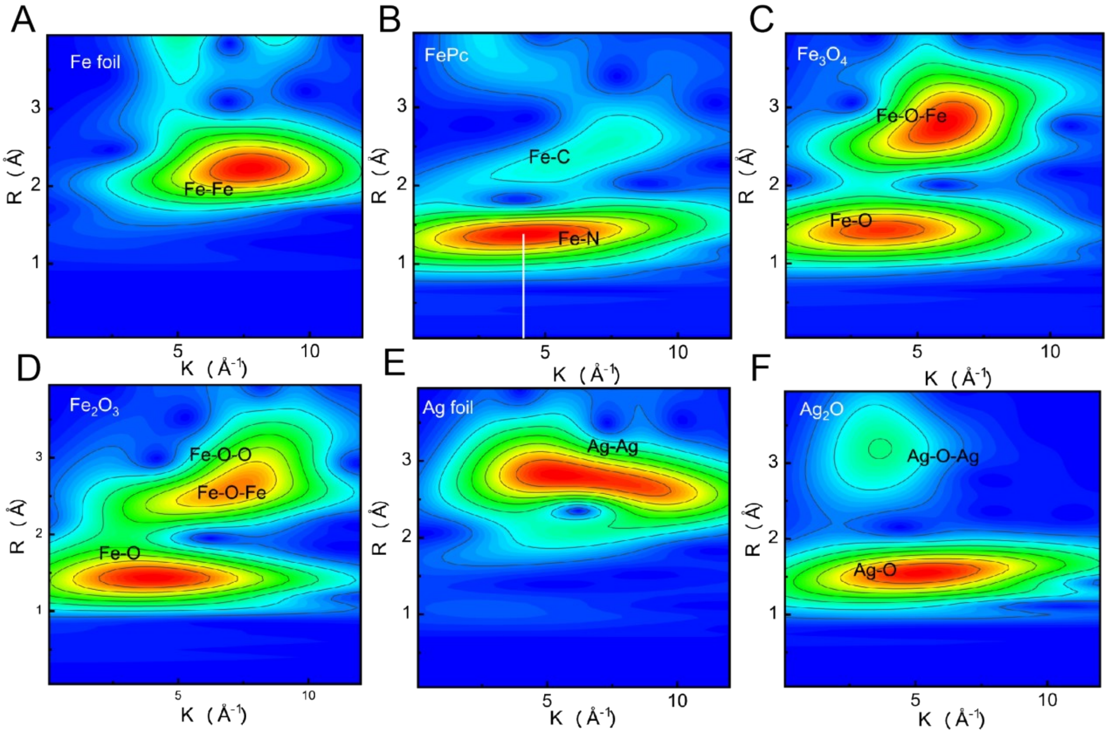

Figure S6 (A-D)wavelet transforms EXANES of the Fe foil, FePc, Fe_3O_4, and Fe_2O_3 as references; (E-F)wavelet transforms EXANES of the Ag foil and Ag_2O as references.

Table S1 EXAFS fitting results of Fe in AgFeAg-N-C

Sample	Path	C.N.	R (Å)	σ^2 (Å^2)	ΔE (eV)	R factor
Fe foil	Fe-Fe	8*	2.47±0.01	0.0051	9.3±0.7	0.0041
	Fe-Fe	6*	2.85±0.01	0.0059		
FeAg-N-C	Fe-N	6.4±0.5	1.95±0.01	0.0071	-5.2±2.0	0.0095
	Fe-C	3.0±1.8	2.78±0.05	0.0059		
	Fe-N-Fe	1.8±0.6	3.05±0.03	0.0069		
FePc	Fe-N	4.3±0.4	1.93±0.01	0.0021	3.5±3.0	0.0163
	Fe-C	8.2±1.7	2.96±0.02	0.0042		
	Fe-N-N	2.4±1.4	3.29±0.04	0.0006		
Fe_3O_4	Fe-O	6.2±0.3	1.99±0.01	0.0126	0.6±0.9	0.0045
	Fe-O-Fe	9.1±0.7	3.02±0.01	0.0160		
	Fe-O-Fe1	8.2±0.6	3.49±0.01	0.0091		
Fe_2O_3	Fe-O	6.3±0.6	1.98±0.01	0.0108	-4.8±1.5	0.0084
	Fe-O-Fe	2.1±0.3	2.92±0.01	0.0014		
	Fe-O-Fe1	4.6±0.6	3.37±0.02	0.0011		
	Fe-O-O1	11.5±2.5	3.54±0.03	0.0033		

Table S2 EXAFS fitting results of Ag in AgFeAg-N-C

Sample	Path	C.N.	R (Å)	σ^2 (Å^2)	ΔE (eV)	R factor

Ag foil	Ag-Ag	12*	2.87±0.01	0.0095	8.1±0.4	0.0057
FeAg-N-C	Ag-N	4.6±0.2	2.18±0.01	0.0152	-5.7±1.6	0.0079
	Ag-N-C	5.5±1.1	3.36±0.02	0.0191		
Ag_2O	Ag-O	2.0±0.1	2.06±0.01	0.0026	4.2±1.0	0.0165
	Ag-O-Ag	12.6±1.7	3.32±0.02	0.0374		

Table S3 The E_{onset} and E_{pc} of FeAg-N-C, Ag-N-C and Fe-N-C

Types of catalysts	E_{onset} / V	E_{pc} / V
Ag-N-C	0.894	0.799
Ag-Fe-N-C	0.959	0.837
Fe-N-C	0.945	0.826

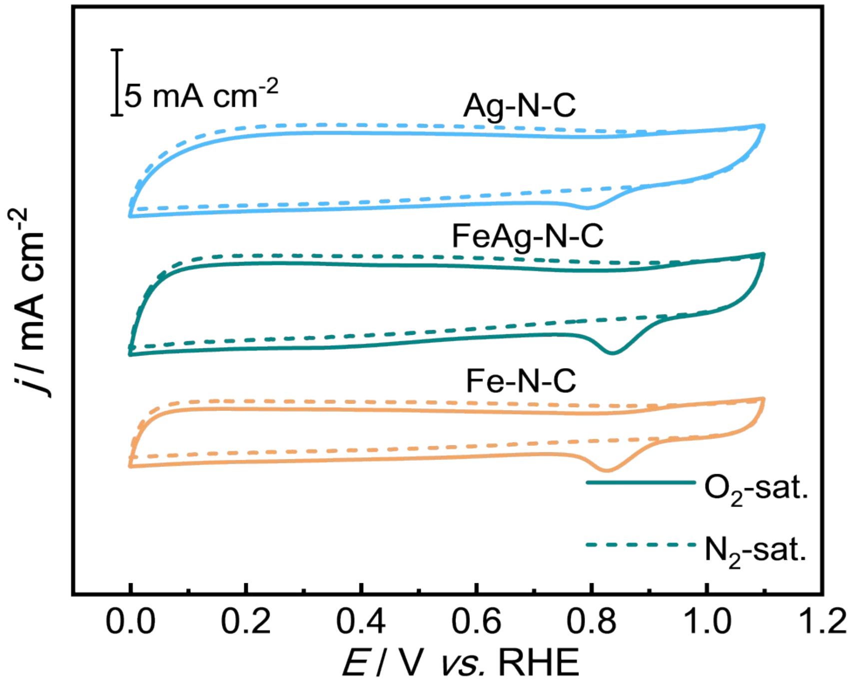

Figure S7 CV curves

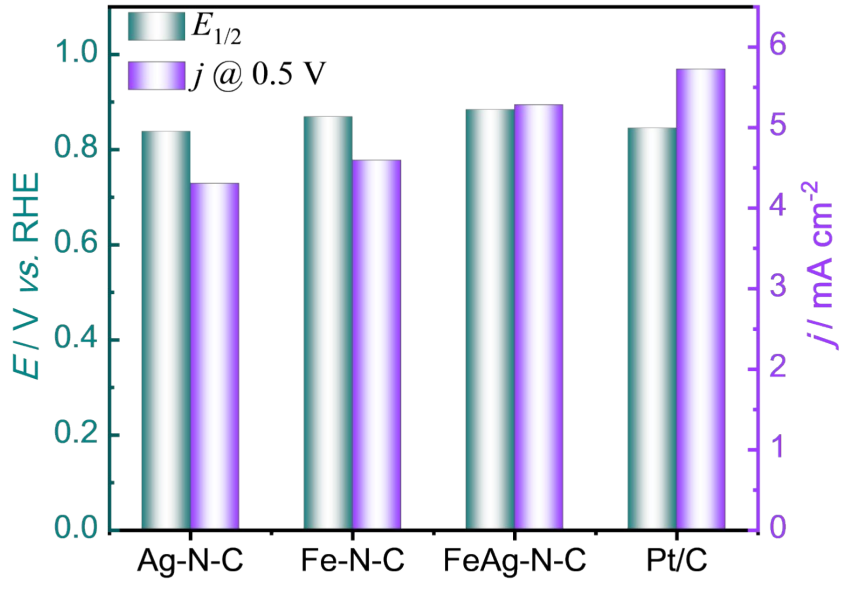

Figure S8 $E_{1/2}$ and J_k (at 0.5 V *vs*. RHE) of the all catalysts and Pt/C.

Table S4 $E_{1/2}$ for ORR and Specific capacity of the battery of FeAg-N-C with some reported Fe- and Ag-based bimetallic catalysts

Catalyst	**$E_{1/2}$ for ORR (V *vs.* RHE)**	**Specific capacity of the battery (mAh g^{-1})**	**Reference**
FeAg-N-C	0.882	833 / (at 50mA cm^{-2})	This work
$Fe_1Co1-N-C$	0.882	750.1 / (at 50mA cm^{-2})	[1]
Fe3C@FeMn-N-C	0.870	815.6 / (10 mA cm^{-2})	[2]
CeO2/Fe3C@N-C	0.926	803 / (at 50mA cm^{-2})	[3]
FeCo/DA@NC	0.84	825 / (10 mA cm^{-2})	[4]
FeSA+AC-N/Se-AHCs	0.90	815 / (at 50mA cm^{-2})	[5]
CuFeDAC-NC	0.89	810.18 / (at 50mA cm^{-2})	[6]
Fe1Te1-900	0.87	810.1 / (at 50mA cm^{-2})	[7]
FeCr-N-C	0.92	789 / (10 mA cm^{-2})	[8]
Fe_2-NC-850	0.78	772 / (20 mA cm^{-2})	[9]
Fe_2Mo/NC	0.91	--	[10]
Ag-Fe-N-C	0.883	--	[11]
Ag/Co/C	0.85	--	[12]
Ag0.1Pd0.9	0.9	--	[13]
P-Ag-Co(OH)2	0.902	--	[14]
Ag/Fe-N-C-2:1	0.78	--	[15]

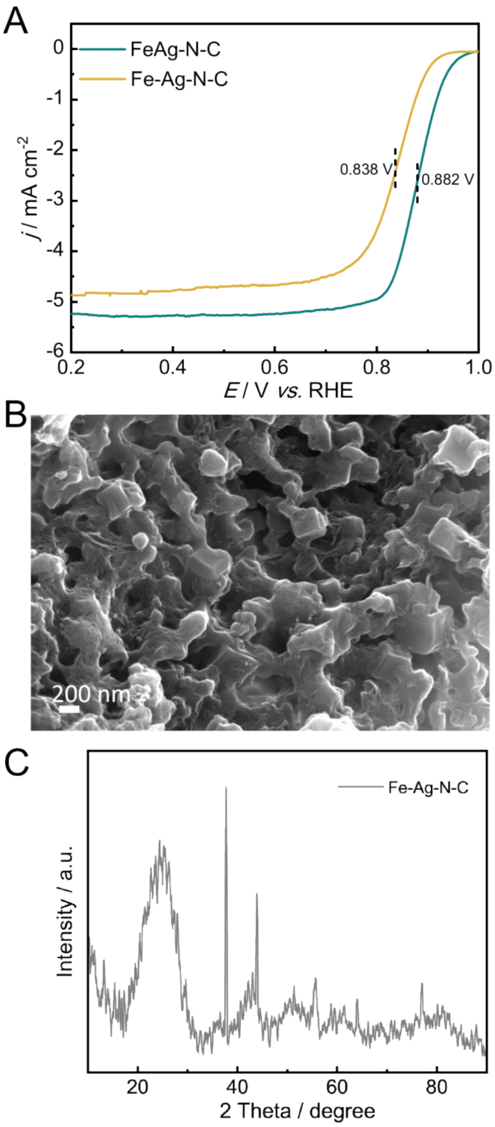

Figure S9 (A) LSVs of different pyrolysis methods; (B) SEM of Fe-Ag-N-C;(C) XRD of Fe-Ag-N-C.

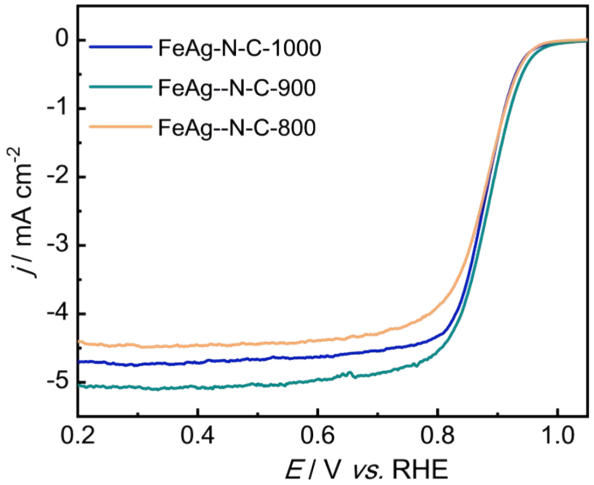

Figure S10 LSVs of different temperatures.

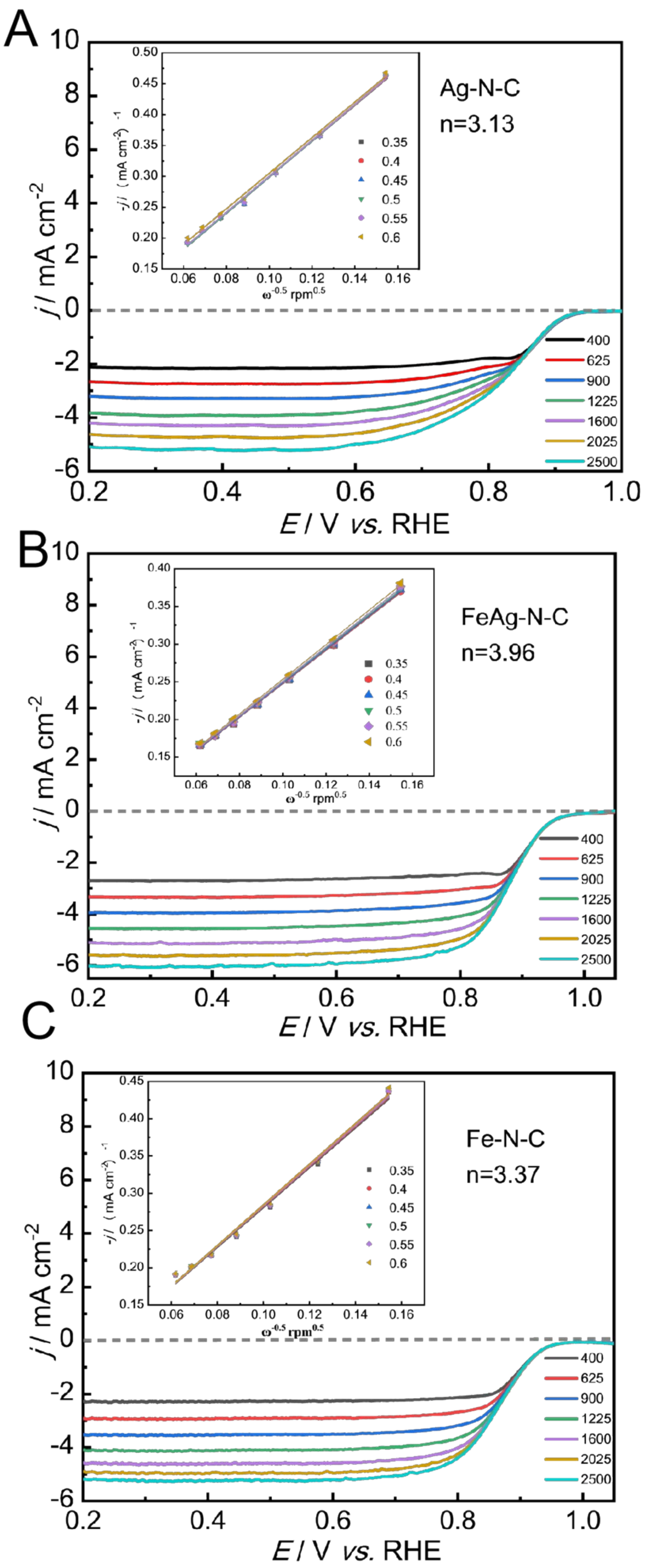

Figure S11 (A-C)LSV curves of FeAg-N-C, Ag-N-C, and Fe-N-C at different scanning rates and K-L curves.

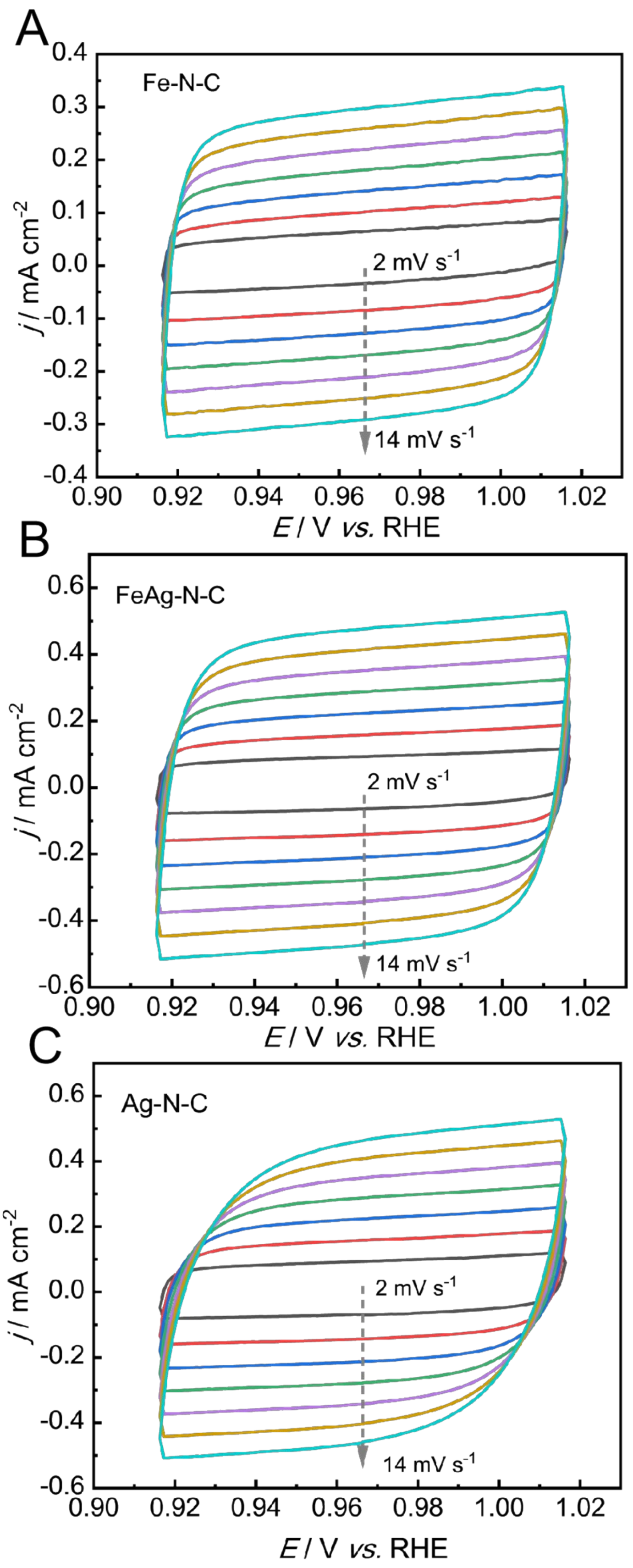

Figure S12 (A-C) CV curves of Fe-N-C, FeAg-N-C, and Ag-N-C at different sweep speeds.

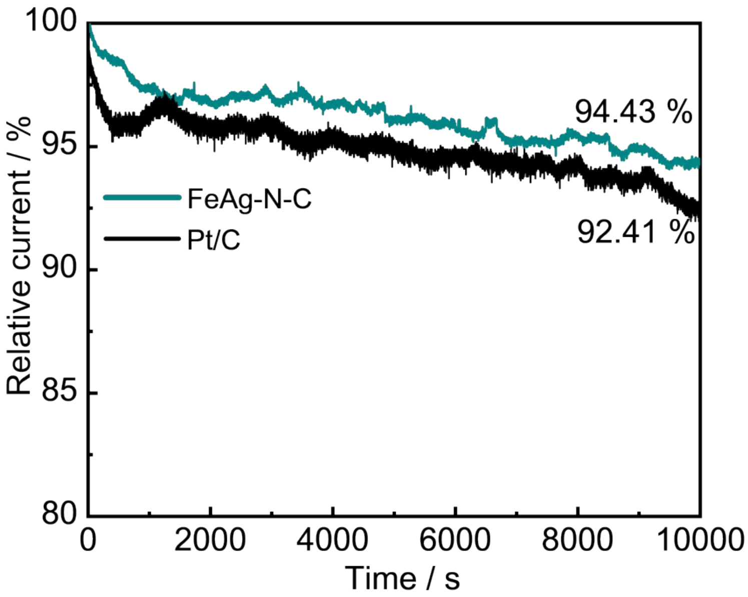

Figure S13 Chronoamperometric response of FeAg-N-C and Pt/C.

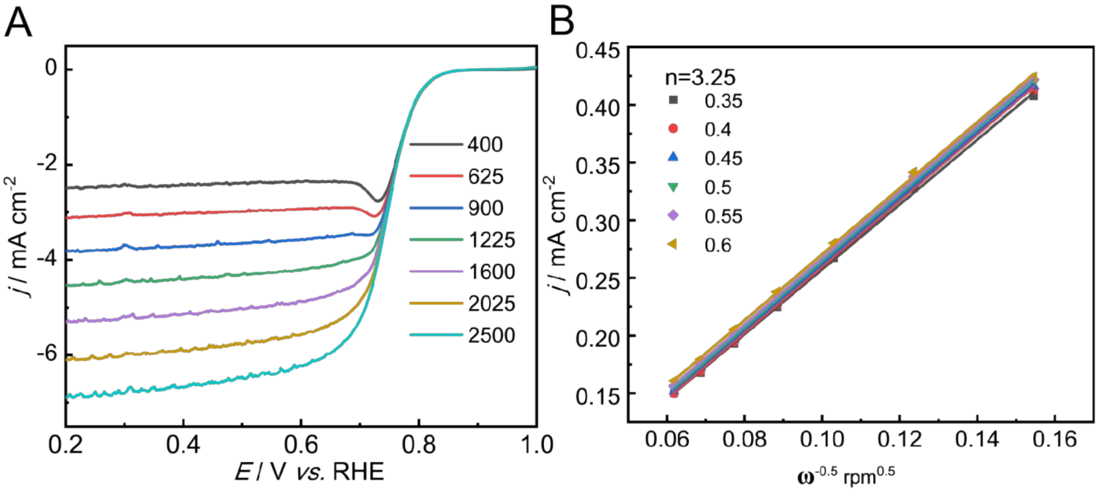

Figure S14 (A-B) LSV curves of FeAg-N-C at different scanning rates in 0.5 M H_2SO_4 solution with saturated O_2 and K-L curves.

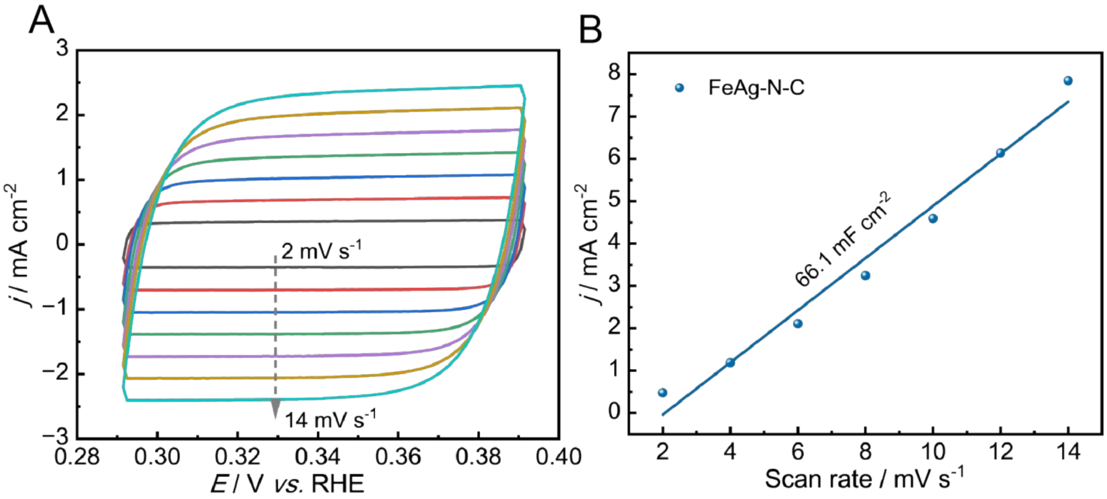

Figure S15 (A-B) CV curve of FeAg-N-C at different sweep speeds in 0.5 M H_2SO_4 solution with saturated O_2 and double-layer capacitance (C_{dl}) .

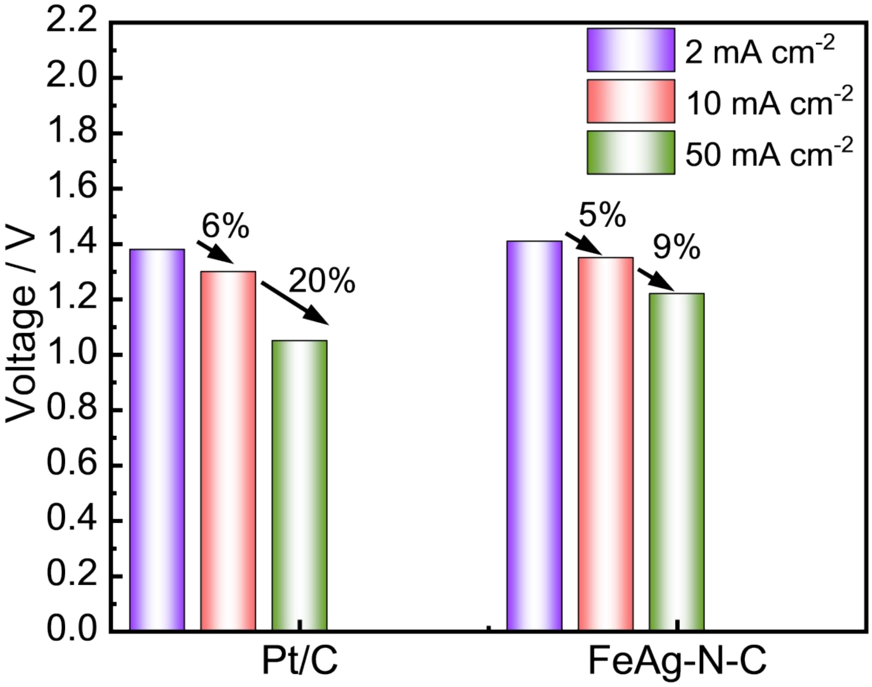

Figure S16 The discharge potentials at 5, 10 and 50 mA cm^{-2} for the FeAg-N-C and Pt/C catalysts, respectively.

Reference

[1] LI T, ZHANG D, ZHANG Y, et al. A pH-dependent microkinetic modeling guided synthesis of porous dual-atom catalysts for efficient oxygen reduction in Zn–air batteries [J]. Energy & Environmental Science, 2025, 18(10): 4949-61.

[2] SHI C, ZHU E, WEI D, et al. Tuning Fe spin state in heteronuclear FeMn-N6 double-site shell by Fe3C core to boost oxygen reduction reaction [J]. Chemical Engineering Journal, 2025, 503: 158679.

[3] WANG P, XU Y, LI Y, et al. Engineering Active CeO2/Fe3C Interfacial Sites to Generate High-Charge-Density Fe for Enhanced Oxygen Reduction Reaction Efficiency [J]. Advanced Functional Materials, 2025: 2503577.

[4] SHENG X, MEI Z, JING Q, et al. Revealing the orbital interactions between dissimilar metal sites during oxygen reduction process [J]. Small, 2024, 20(7): 2305390.

[5] SUN J, SHEN M, JUN CHANG A, et al. Asymmetric Fe-N3Se single atoms coupled with Fe atomic clusters on alveolar-inspired hierarchically porous carbon submicronspheres for enhanced oxygen reduction [J]. Applied Catalysis B: Environment and Energy, 2025: 126102.

[6] LIU C, SHI W, YUAN Y, et al. Cascade Hydrogen Peroxide Reduction Reaction Endows Cu-Fe Dual-Atom Catalyst with Durable Oxygen Reduction Performance [J]. Advanced Functional Materials, 2025: 2503079.

[7] LI Z, LIU S, KANG W, et al. Engineering the Local Atomic Environments of Te-Modulated Fe Single-Atom Catalysts for High-Efficiency O2 Reduction [J]. Small, 2025, 21(2): 2406659.

[8] WANG J, ZHANG Q, YANG L, et al. Interfacial hydrogen bonds induced by porous FeCr bimetallic atomic sites for efficient oxygen reduction reaction [J]. Journal of Colloid and Interface Science, 2025, 683: 742-51.

[9] CUI J, ZHANG W, HOU Y, et al. Geminal Cl-Bridged Dual-Fe-Atom Catalyst for Efficient and Stable Oxygen Reduction Reaction [J]. Journal of the American Chemical Society, 2026.

[10] HU J, ZHANG C, SUN M, et al. Ultrastable bimetallic Fe2Mo for efficient oxygen reduction reaction in pH-universal applications [J]. Nano Research, 2022, 15(6): 4950-7.

[11] JIN R, WU G-G, XU C, et al. Enhancing oxygen reduction on a bimetallic Ag-Fe-NC electrocatalyst for a zinc-air battery [J]. Journal of Alloys and Compounds, 2023, 967: 171673.

[12] MURAD M, KHAN S, KHAN N A, et al. A review of transition metal compounds-carbon hybrid electrocatalysts for sustainable hydrogen production through water splitting [J]. Reviews in Inorganic Chemistry, 2025, (0).

[13] ZAMORA ZELEDóN J A, STEVENS M B, GUNASOORIYA G K K, et al. Tuning the electronic structure of Ag-Pd alloys to enhance performance for alkaline oxygen reduction [J]. Nature communications, 2021, 12(1): 620.

[14] LI Z, KANG W J, LIU H, et al. Ag anchored atomically around nanopores of porous Co (OH) 2 for efficient bifunctional oxygen catalysis [J]. Advanced Functional Materials, 2023, 33(34): 2301947.

[15] ZHONG K, HUANG L, LI H, et al. Enhanced oxygen reduction upon Ag/Fe co-doped UiO-66-NH2-derived porous carbon as bacteriostatic catalysts in microbial fuel cells [J]. Carbon, 2021, 183: 62-75.